Experimental Validation of an Efficient Fan-Beam Calibration Procedure for k-Nearest Neighbor Position Estimation in Monolithic Scintillator Detectors

Giacomo Borghi, *Student Member, IEEE*,
Valerio Tabacchini, Stefan Seifert, and Dennis R. Schaart, *Senior Member, IEEE*

Abstract—**Monolithic scintillator detectors can achieve excellent spatial resolution and coincidence resolving time. However, their practical use for positron emission tomography (PET) and other applications in the medical imaging field is still limited due to drawbacks of the different methods used to estimate the position of interaction. Common statistical methods for example require the collection of an extensive dataset of reference events with a narrow pencil beam aimed at a fine grid of reference positions. Such procedures are time consuming and not straightforwardly implemented in systems composed of many detectors. Here, we experimentally demonstrate for the first time a new calibration procedure for k-nearest neighbor (k-NN) position estimation that utilizes reference data acquired with a fan beam. The procedure is tested on two detectors consisting of 16 mm $\times$ 16 mm $\times$ 10 mm and 16 mm $\times$ 16 mm $\times$ 20 mm monolithic, Ca-codoped LSO:Ce crystals and digital photon counter (DPC) arrays. For both detectors, the spatial resolution and the bias obtained with the new method are found to be practically the same as those obtained with the previously used method based on pencil-beam irradiation, while the calibration time is reduced by a factor of $\sim$ 20. Specifically, a FWHM of $\sim$ 1.1 mm and a FWTM of $\sim$ 2.7 mm were obtained using the fan-beam method with the 10 mm crystal, whereas a FWHM of $\sim$ 1.5 mm and a FWTM of $\sim$ 6 mm were achieved with the 20 mm crystal. Using a fan beam made with a $\sim$ 4.5 MBq ^{22}Na point-source and a tungsten slit collimator with 0.5 mm aperture, the total measurement time needed to acquire the reference dataset was $\sim$ 3 hours for the thinner crystal and $\sim$ 2 hours for the thicker one.**

Index Terms—**Calibration, fan beam, monolithic scintillator detector, nearest neighbor method, PET, positron emission tomography.**

I. INTRODUCTION

G AMMA-RAY detectors based on bright monolithic scintillation crystals such as L(Y)SO:Ce(Ca) and LaBr$_3$:Ce coupled to position-sensitive light sensors such as multi-anode

photomultipliers tubes (PMTs), arrays of avalanche photodiodes (APDs) and silicon photomultipliers (SiPMs) are currently being investigated for several applications in the medical imaging field. Mainly, these detectors have been considered for small-animal positron emission tomography (PET) [1]–[5] and dedicated PET systems [6]. However, monolithic crystals are also considered for clinical PET [7] and Compton cameras for dose monitoring during hadron therapy treatments [8]. Moreover, advances in gamma-ray detectors can be applied in single photon emission computed tomography (SPECT) [9].

Monolithic scintillator detectors have already shown the capability to achieve good spatial resolution and excellent timing resolution even with thick ($\sim$ 15 mm $-$ 20 mm) crystals. For example, several research groups have obtained spatial resolutions better than 2 mm FWHM in crystals with a thickness of 10 mm - 15 mm [10]–[12], while coincidence resolving times (CRT) well below 200 ps FWHM have recently been achieved with 10 mm and 20 mm thick LSO:Ce(Ca) crystals [13]. Moreover, monolithic scintillator detectors provide good energy resolution [11], [14], show better sensitivity compared to high-resolution crystal matrices due to the absence of dead space, and can estimate the depth of interaction (DOI) from the shape of the light distribution [15]–[20]. In fact, the main advantage of detectors based on continuous crystals is that they can provide all of these results simultaneously, whereas detectors based on pixelated crystals typically require a tradeoff between spatial resolution on the one hand and sensitivity, time resolution and energy resolution on the other.

At present, the practical use of monolithic scintillator detectors is still hampered by drawbacks of the different techniques used to estimate the position of interaction, which can be broadly subdivided into two classes: parametric methods and statistical methods. The first class comprehends the positioning algorithms based on modelling of the relation between the 3D position of the light source inside the crystal and the light distribution measured by the photosensor [17], [19]. The main advantage of these methods is that they need little or no calibration data, since they are based on geometrical and physical considerations. However, these models usually have difficulties in positioning events close to the edges of the crystals, due to the truncation of the measured light distribution [17] and might not be robust in case of

non-ideal response of the detectors. Also, they require quite intensive computational power, since for each unknown event a function with several fitting parameters has to be minimized or maximized. Moreover, to our knowledge, they have not yet been demonstrated for crystals thicker than 10 mm.

Common statistical methods include maximum likelihood (ML) positioning [16], [18], neural networks [21], [22], and the k-nearest neighbor (k-NN) method [2], [23]. These position estimation techniques are based on a thorough experimental characterization of the detector response as a function of the gamma-photon incidence position, which is usually performed by irradiating the detectors at precise positions with a narrowly collimated pencil beam of annihilation photons. These methods take into account the non-ideal response of the individual detector as well as the statistical properties of the signals, either incorporating them in a model (ML) or finely sampling the possible response for the same class of events (k-NN and neural networks). These methods can achieve excellent positioning performance. However, the complex and time demanding calibration procedures needed to acquire a set of reference events still impose a significant drawback for their application. Moreover, ML positioning and k-NN algorithms also require intense computational power.

Recently, a new statistical position estimation approach based on self-organizing maps (SOMs) was demonstrated by España, *et al.*, in a 5 mm thick NaI(Tl) monolithic scintillator detector for SPECT [9]. This method employs reference events acquired by flood irradiation and therefore requires a calibration measurement considerably more practical than other approaches. However, this SOM technique has been demonstrated only for estimating the 2D position of interaction of low-energy (141 keV) photons in thin crystals and thus has not yet been demonstrated for PET applications.

In this work, we focus on the k-NN method that is known to give good results in monolithic scintillator PET detectors [11], [14], [24], [25]. An early implementation of the k-NN method [2] made use of multiple reference datasets, each acquired at a different angle of incidence on the detector. Although this approach had the ability to estimate the entry point of the gamma-ray, thus avoiding parallax errors resulting from depth of interaction (DOI) variations, the total number of reference events required was very large.

More recently it was shown that the DOI in monolithic scintillators can be estimated directly based on the shape of the measured light distribution [20]. This approach requires only perpendicular calibration events and thus makes it possible to use a single perpendicular reference dataset both for training the DOI classifier and for estimating the $x-y$ position of interaction using the k-NN method. This DOI estimation method thus removes the need to acquire reference events at multiple angles of incidence and reduces the time needed for detector calibration substantially.

Further acceleration of the k-NN approach was achieved by Van Dam, *et al.* [23], who reported on a number of modified k-NN methods that required a significantly smaller amount of reference data than the standard k-NN method while giving similarly good results. However, the reference events were still collected with a narrow pencil beam aimed at a fine grid of refer-

ence positions covering the entire crystal surface. Implementation of this approach in a completely assembled clinical or preclinical PET system is not straightforward. Similar pencil-beam calibration is also used with ML methods and methods based on neural networks, which therefore suffer from the same practicality problem.

Van Dam, *et al.*, therefore suggested, but did not experimentally test, a potential approach to further speed up and facilitate the calibration process [23]. They described how an adaptation of the k-NN algorithm might enable the use of reference events acquired with a line source or a fan beam. Due to the higher count rate obtained with a fan beam, the acquisition of calibration events could be much faster. In addition, it was foreseen that fan beams could be realized in a practical way within clinical scanners, e.g. through electronic or mechanical collimation of line sources.

Here, k-NN estimation of the position of interaction in monolithic scintillator detectors utilizing reference data acquired with a fan beam is tested experimentally for the first time. The spatial resolution obtained with this new approach is compared to that obtained with pencil beams in order to determine if fan-beam irradiation can be considered a valid option for the calibration of monolithic scintillators.

II. MATERIAL AND METHODS

A. Experimental Setup

Digital Silicon Photomultiplier Array: The detectors used in this work were based on Digital Photon Counter (DPC) arrays (version DPC-3200-22-44), a type of digital silicon photomultiplier (dSiPM) array developed by Philips Digital Photon Counting (PDPC). This array measures 32.6 mm $\times$ 32.6 mm and consists of 4×4 autonomous sensors (dies), each divided into 2×2 pixels. Each pixel comprises a total of 3200 microcells arranged into 64 columns and 50 rows, grouped into 2×2 equal sub-pixels.

Each DPC microcell is composed of a single photon avalanche photodiode (SPAD) and logic circuitry that actively quenches and recharges the SPAD after a discharge. The circuitry is also used to read out the state of the SPAD and can enable or disable it, giving the possibility to switch off the diodes that show an abnormally high dark count rate (DCR). A more detailed description of the DPC array can be found in [26], [27].

The acquisition sequence of a die is started by a trigger, whose threshold can be set by the user. In this work, the trigger level $MT_{=1}$ was used, i.e. a trigger is generated every time that a single cell discharges on the die. Whenever a trigger is generated, a time stamp is acquired and the die goes into the validation phase. During this phase, the sensor waits for a user-selected time interval and then checks if a higher threshold criterion, also selected by the user, is reached. In this work, the validation interval was set to 20 ns. The validation threshold was set such that the event is acquired if at least one pixel has at least one fired cell on each of its sub-pixels (DPC threshold notation: '0x7F:AND'). If none of the pixels reaches the validation criterion, the die undergoes to a fast recharge and reset, which takes about

20 ns. If the die is validated, the acquisition sequence is completed. First, the die waits for a user-defined integration time, which in this work was set to 165 ns. Afterwards, during the readout phase (680 ns), the number of fired cells is counted row-by-row and the summed number of cells per pixel is acquired. Finally, a recharge and reset sequence is performed. Therefore, when an event is acquired, a die provides one time stamp as well as the number of fired cells on each of its pixels.

Before the detectors were assembled, the DCR of the DPC arrays used in this work was measured at the temperature used for the measurements ($-25°C$). The measurement was performed following the procedure described in [26] and was used to disable the noisiest 5% of the cells.

Monolithic Scintillator Detectors: Two monolithic scintillator detectors were tested in this work. These detectors were assembled using Ca-codoped (0.2% in the melt) LSO:Ce crystals [28], which were produced at the Scintillation Materials Research Center, University of Tennessee and provided by Agile Engineering Inc. (Knoxville, TN, USA). The crystals had polished surfaces, a base area of 16 mm × 16 mm and a thickness of 10 mm or 20 mm.

The scintillators were positioned on the four central dies of a DPC array (covering 4 × 4 pixels in total) and were optically coupled to the photosensor using a transparent silicone material (Sylgard 527, Dow Corning). In both cases, the four lateral faces of the crystal were covered with a specular reflector foil (Vikuiti ESR, 3M), whereas the top face was covered with Teflon tape. A coincidence detector was assembled using the same procedure with a standard LSO:Ce crystal (Agile Engineering Inc., Knoxville, TN, USA) having dimensions of 16 mm × 16 mm × 20 mm.

Measurement/Irradiation Setup: A paired-collimator system was designed in order to obtain the 511 keV annihilation-photon beams needed to calibrate and test the detectors. This system is based on a central tungsten housing that contains an encapsulated ^{22}Na point-source ($\emptyset$ 0.5 mm, ∼ 4.5 MBq, IDB Holland BV), surrounded in each direction by at least 3 cm of tungsten or lead (Fig. 1, Fig. 2). On one side of this housing, two different 80 mm long tungsten collimators can be mounted in order to define the beam used to irradiate the detector under test. On the other side, two corresponding 70 mm long lead collimators are used to reduce the count rate on the reference detector and to minimize the chance of random coincidences.

The first tungsten collimator has a cylindrical aperture having a diameter of 0.5 mm and it is paired to a lead collimator which has a 3 mm diameter cylindrical aperture (Fig. 1). This set of collimators is used to create a narrow pencil beam for which both the x and y positions of interaction of the gamma-photons in the irradiated crystal are accurately known.

The second tungsten collimator has a rectangular aperture 0.5 mm wide and ∼ 35 mm long (Fig. 2). Its paired lead collimator, instead, has a trapezoidal aperture, which is 3 mm wide and ∼ 29 mm long on the side further from the source.

This set of collimators is used to obtain a fan beam. Since the whole collimator system can rotate by an angle of $90°$, the fan beam can be aligned perpendicularly to the x or y axis of the detector under test (Fig. 3). In this manner, the x or y position of
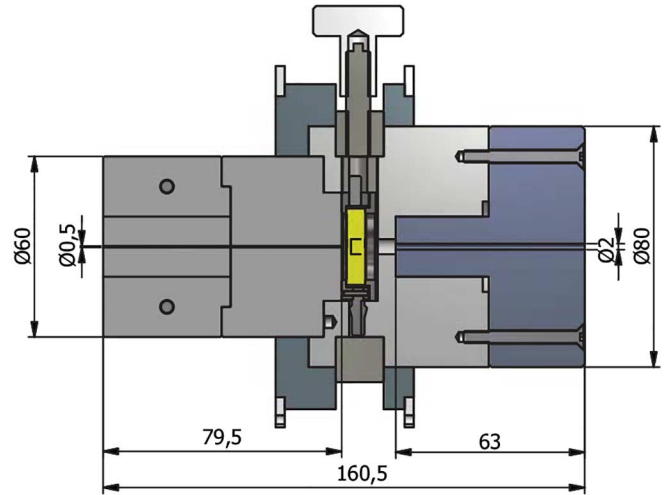

Fig. 1. Design of the collimator used to create a pencil beam having a diameter of 0.5 mm (all dimensions in mm).
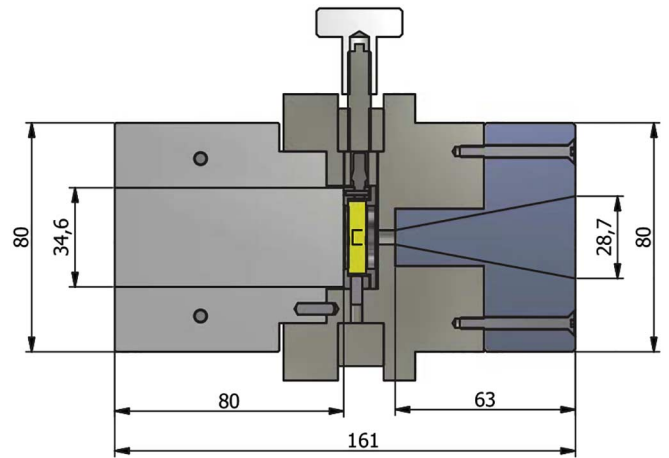

Fig. 2. Design of the collimator used to create the fan beam having a width of 0.5 mm (all dimensions in mm).

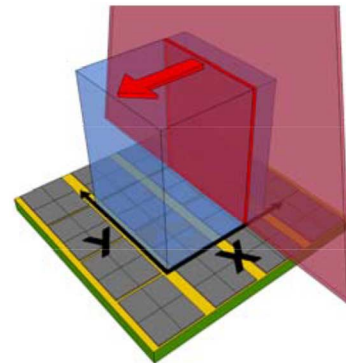Fig. 3. Illustration of the acquisition of the x-reference dataset with a fan beam. The narrow fan beam is aligned perpendicularly to the x axis and moved in the small steps along the x direction. For each x position a fixed number of event is acquired.

interaction of the gamma-photons in the crystal is known, while the fan beam irradiates the crystal approximately uniformly in the other direction.

The detectors to be tested were fixed on two linear $x - y$ stages with a range of 100 mm and a precision $\leq 10\ \mu$m, driven by stepper-motors (Physics Instruments, M-403.42S stages with C-663 controllers). These stages were used to move the detectors in the plane perpendicular to the beam direction and to automatically acquire the reference/test events in all required positions.

The setup was assembled inside a light-tight temperature chamber (Weiss WT 450/70). To reduce the DCR on the sensors, the ambient temperature was set to $-25°$C. In order to dissipate the heat produced by the dSiPMs during operation, Peltier elements were coupled to the backsides of the sensors. The Peltier elements were regulated by a PI (proportional-integral) feedback system keeping the detector temperature stable within $\sim 0.1°$C.

B. Data Acquisition

Two different sets of events were acquired for each detector. The first set was obtained by irradiating the entire front surface of the crystals with the pencil beam at a grid of 64×64 reference positions, at a pitch of 0.25 mm. For each point, 250 events were registered for which all the dies below the crystal were acquired and the full 511 keV energy was deposited. The energy selection was performed by creating an energy spectrum of the events acquired on all the positions and considering only the interactions comprised in the full width at tenth maximum (FWTM) of the photo-peak.

The second set was obtained by irradiating the crystals with the fan beam. First, the fan beam was aligned perpendicularly to the crystal x-axis and measurements were acquired at a series of 64 reference positions spaced 0.25 mm apart along the x-direction. At each position, 6400 full-energy, all-dies events were registered in order to obtain a first subset, hereafter referred as the x-subset. Subsequently, the fan beam was rotated by 90° and the y-subset was acquired using a similar procedure.

The light distributions of the events acquired with both of the irradiation methods were normalized to the sum of all pixel values before further processing and analysis.

C. Data Processing and Analysis

Position Estimation: Four position estimation methods were used in this study, all based on the k-NN algorithm. Two established methods using reference dataset acquired with a pencil-beam irradiation were used as a benchmark for the methods based on fan-beam calibration [23]:

i) Standard k-NN (Max 2D). This method calculates the Euclidean distance of the light distribution of the unknown event to those of all the events in the reference dataset. The k reference events having the smallest distances (nearest neighbors) are selected and a 2D histogram of their (x, y) irradiation coordinates is subsequently made. The position of the unknown events is estimated as the position of the 2D histogram for which there is the maximum number of entries. In case of multiple maxima, one of them is selected randomly.

ii) Smoothed k-NN (Smoothed 2D). This method is similar to the standard one but a moving average filter is used to smooth the 2D histogram of the coordinates of the k nearest neighbors before locating the maximum. The

filter is a square $n \times n$ filter which is cropped at crystal edges when necessary. In this work $n = 5$; therefore in the Smoothed 2D histogram each bin is the average of an area of 25 bins of the original histogram, except at the crystal borders.

The two methods based on a fan-beam irradiation are:

iii) Standard k-NN 1D (Max 1D). To determine x, this method calculates the Euclidean distance between the light distribution of the unknown event and those of all events contained in the x-subset. The k events having the most similar light distributions are selected and a 1D histogram of their x coordinates is made. The x coordinate of the unknown event is estimated as the position in the histogram that has the most entries. In case of multiple maxima, one of them is selected at random. The procedure is then repeated to estimate the y coordinate using the y-subset.

iv) Smoothed k-NN 1D (Smoothed 1D). The position estimation is performed similarly as for the 1D Max method, except that the 1D histograms are smoothed with a moving average filter that is n bins wide. When the filter approaches the edges of the histogram, its dimensions are reduced on the edge side. In this work, $n = 5$.

For both crystals, the entire dataset acquired with the pencil beam (250 events per grid position) was used as a test set and the positions of all events were estimated using the four different methods.

For the Max 2D and the Smoothed 2D algorithms, part of the same pencil-beam dataset was used as reference set, namely 100 fixed events per position. Whenever the positions of events belonging to the reference set were estimated, the leave-one-out method described in [24] was applied, whereas in all other cases the entire reference set was used.

For the Max 1D and the Smoothed 1D algorithms, the x- and y-subsets acquired with the fan beam, containing 6400 events per position, were used as reference set. Each subset, therefore, had the same number of events included in the pencil-beam reference dataset.

Since the fan beam is obtained by mechanical collimation of a point source, the crystal is not irradiated truly perpendicularly and uniformly along the entire length of the irradiated line. The uniformity of the acquired reference events along this line is additionally compromised by the increased escape probability of the scattered photon following a Compton interaction in the neighborhood of a crystal edge. To verify the influence of these effects, the Max 1D and the Smoothed 1D algorithms were additionally tested with an idealized 1D reference dataset containing perpendicularly incident events distributed uniformly along the irradiated line. This idealized fan-beam dataset is constructed from the pencil-beam dataset used as a reference for the 2D position estimation methods by alternately grouping together all events with the same x or y position on the grid. These experiments are referred to as Max 1D$_{ideal}$ and Smoothed 1D$_{ideal}$, respectively.

For all methods, the position estimation was performed selecting the 100 closest matches ($k = 100$) for building the 1D or 2D histograms of the nearest neighbors. Both the number of

reference events and the number of closest matches were optimized in order to approach the best achievable results without excessively increasing the reference dataset.

Misalignment Correction: Before each measurement, a procedure based on count rate profiles was performed to align the collimator and the detector under test. The alignment procedure defines a coordinate system using the edges of the crystal as a reference. However, small differences in the alignments performed for different measurements (in the order of $0.1 - 0.2$ mm) cannot be avoided completely. If the coordinate systems used to acquire test and reference events are not perfectly aligned, this may result in a bias when the accuracy of the position estimation is checked.

In this work, no bias is expected for the 2D and the 1D$_{ideal}$ methods, since the test and reference events are acquired during the same measurement. However, for the Max 1D and the Smoothed 1D methods the test events and reference events are acquired separately. Therefore, a procedure was developed to compare the alignment of the coordinate system used during fan-beam irradiation with the coordinate system used during pencil-beam irradiation and, if necessary, to correct for their differences. This procedure is described in Appendix A.

Spatial Resolution: Detector point spread functions (PSFs) were determined as the normalized 2D histograms of the differences between the estimated positions of the test events and their true irradiation coordinates. The measures that are used for the x and y spatial resolution are the full width at half maximum (FWHM) and the full width at tenth maximum (FWTM) of the corresponding cross-sections of the PSF through its maximum.

For each of the two detectors, in combination with each of the six position estimation methods, the whole-detector PSF (containing the errors of all test events acquired over the entire detector surface) was built. The overall spatial resolutions were then estimated by interpolating the PSF cross-sections with a 1D cubic spline. For the Max 1D and the Smoothed 1D methods, the PSFs were built after applying the misalignment correction described in Appendix A.

In previous research, it has been shown that the spatial resolution of monolithic scintillator detectors depends on the position of interaction and usually degrades towards the edges of the crystal [11], [14], [24]. This problem was investigated for fan-beam calibration and compared with a standard position estimation method. To this end, a detailed analysis of small regions of the crystals was performed for both detectors, considering only the Smoothed 1D and the Smoothed 2D methods. Specifically, the front surface of the crystals was divided into six different regions, shown in Fig. 4, and for each region a separate PSF was built. The regional FWHM and FWTM were then calculated and used to compare the different calibration methods.

Bias: For both crystals, the bias in the position estimation obtained with the Smoothed 1D and the Smoothed 2D methods were analyzed. This study was performed using a method similar to the one described in [11], [14]. For each irradiation position $\boldsymbol{v}_{ij}$, the bias vector $\boldsymbol{b}(\boldsymbol{v}_{ij})$ was calculated as the mean error of the estimated positions:

$$\boldsymbol{b}\left(\boldsymbol{v}_{i,j}\right) = \begin{bmatrix} \frac{\sum_{m=1}^{M}(\hat{x}_m(\boldsymbol{v}_{i,j})-x_{i,j})}{M} \\ \frac{\sum_{m=1}^{M}(\hat{y}_m(\boldsymbol{v}_{i,j})-y_{i,j})}{M} \end{bmatrix}, \qquad (1)$$
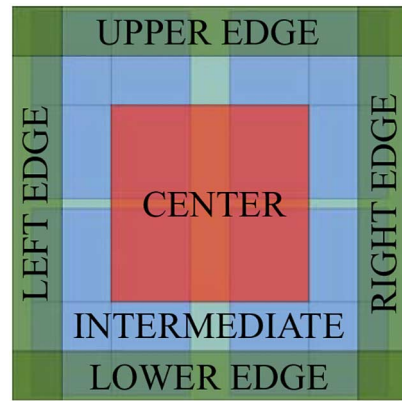

Fig. 4. The different regions defined to study the variation of the spatial resolution and bias across the detector area. The center region is 8 mm × 8 mm wide and the edge regions are defined as the 2 mm borders on each side of the crystal. The intermediate region is the area not covered by the center and edge regions.

where m is the mth test event acquired at position $\boldsymbol{v}_{i,j} = (x_{i,j}, y_{i,j})$ (i and j being the row and column indexes of the grid), $\boldsymbol{v}_m^{\hat{}} = (\hat{x}_m, \hat{y}_m)$ is its estimated position and M is the number of events per positions.

No further selection was made on the estimated events, so, for each point, $M = 250$. The crystal surface was divided in areas 0.5 mm × 0.5 mm wide, each containing four irradiation points, and the average bias vector was calculated for each of them. The vector magnitudes were calculated as their Euclidean norm.

III. RESULTS AND DISCUSSION

A. Calibration Time

The coincidence event rate measured during fan-beam irradiation equals ~ 200 Hz for the 10 mm thick crystal and ~ 300 Hz for the 20 mm thick one. In both cases this is ~ 40 times higher than the coincidence event rate registered with the pencil beam, as expected from the ratio of the different irradiated areas. Since the x- and y-subsets acquired with the fan beam contain the same number of events as the pencil-beam reference set (see Section II-B), the fan-beam calibration procedure is ~ 20 times faster for 16 mm × 16 mm crystals. It has to be emphasized that the same point source was used for both measurements and only the paired collimators were changed. The measurement time needed to acquire the total fan-beam dataset was ~ 3 hours for the thinner crystal and ~ 2 hours for the thicker one.

B. Spatial Resolution

The overall spatial resolutions obtained with the six different position estimation methods (see Section II-C) are reported in Table I and Table II for the 16 mm × 16 mm × 10 mm and the 16 mm × 16 mm × 20 mm crystal, respectively. Using the fan-beam (Smoothed 1D) method, a FWHM of ~ 1.1 mm and a FWTM of ~ 2.7 mm were obtained with the thinner crystal in both the x and y directions. With the 20 mm thick crystal, the fan-beam method resulted in a FWHM of ~ 1.5 mm and a FWTM of ~ 6 mm.

For both detectors, the results were practically the same as those obtained with the pencil-beam (Smoothed 2D) method.

TABLE I
OVERALL SPATIAL RESOLUTIONS OBTAINED WITH THE POSITION ESTIMATION METHODS DESCRIBED IN SECTION II-C) FOR THE 16 mm × 16 mm × 10 mm CRYSTAL

METHOD	BEAM	X DIRECTION		Y DIRECTION	
		FWHM (mm)	FWTM (mm)	FWHM (mm)	FWTM (mm)
Max 2D	Pencil	1.25	3.05	1.27	3.17
Smoothed 2D	Pencil	1.07	2.63	1.07	2.75
Max 1D$_{ideal}$	Pencil	1.17	2.88	1.18	2.98
Smoothed 1D$_{ideal}$	Pencil	1.07	2.67	1.06	2.78
Max 1D	Fan	1.21	2.88	1.21	2.97
Smoothed 1D	Fan	1.08	2.70	1.10	2.75

TABLE II
OVERALL SPATIAL RESOLUTIONS OBTAINED WITH THE POSITION ESTIMATION METHODS DESCRIBED IN SECTION II-C) FOR THE 16 mm × 16 mm × 20 mm CRYSTAL

METHOD	BEAM	X DIRECTION		Y DIRECTION	
		FWHM (mm)	FWTM (mm)	FWHM (mm)	FWTM (mm)
Max 2D	Pencil	1.92	6.66	1.91	7.30
Smoothed 2D	Pencil	1.49	5.85	1.50	6.22
Max 1D$_{ideal}$	Pencil	1.73	6.40	1.79	6.63
Smoothed 1D$_{ideal}$	Pencil	1.54	6.02	1.57	6.22
Max 1D	Fan	1.77	6.50	1.84	7.30
Smoothed 1D	Fan	1.51	5.94	1.57	6.38

Moreover, the smoothing procedure appears to significantly improve the positioning accuracy compared to the Max 1D method, similar to what was found for the corresponding 2D algorithms [23].

The results obtained with the Max 1D$_{ideal}$ and Smoothed 1D$_{ideal}$ datasets (see Section II-C) are essentially equal to those achieved using the corresponding datasets obtained with the mechanically collimated fan beam (Max 1D and Smoothed 1D, respectively). This indicates that a reference dataset acquired with a realistic fan beam performs similarly well as a dataset acquired under idealized conditions, i.e. with all reference events incident perpendicularly to the crystal and distributed uniformly along the irradiated line.

The FWHM and FWTM values obtained from the regional PSFs are given in Table III and Table IV for the 10 mm and 20 mm thick crystals, respectively. For the thinner crystal, the Smoothed 1D method yields FWHM values comparable to the Smoothed 2D method in almost all cases. Only in the edge regions slightly worse FWHM values are found for the coordinate perpendicular to the edge considered. In most of the crystal regions, the 1D method furthermore yields slightly (0.1 mm − 0.2 mm) higher values of the FWTM. However, the differences are small and the two methods can be assumed to be substantially equivalent.

The FWHM values obtained in the edge regions of the 20 mm thick crystal show similar trends as in the 10 mm thick one. As for the FWTM values, their comparison becomes more difficult for this detector, since the PSFs are wider and therefore suffer from statistical fluctuations on their tails. However, a trend for slightly higher FWTM values for the 1D position estimation

method can again be noticed, which in any case does not substantially deteriorate the positioning performance.

The actual shapes of the PSFs obtained with 1D and 2D position estimation are also found to be practically equivalent. As an example, a comparison of the cross-sections in the y-direction of the PSFs obtained in four selected regions are shown in Fig. 5 for the 10 mm thick crystal and in Fig. 6 for the 20 mm thick one. These findings demonstrate that the new 1D position estimation procedure based on calibration data acquired with a fan beam can achieve results similarly good as the method using pencil-beam calibration data.

The results obtained here with a 16 mm × 16 mm × 10 mm LSO:Ce,0.2%Ca crystal mounted on a DPC-3200-22-44 array are similar to the best values reported in literature for ∼ 10 mm thick crystals. Seifert et al., for example, in [11] characterized a detectors similar to the one presented in this work, which was based on a 24 mm × 24 mm × 10 mm LSO:Ce,0.2%Ca crystal coupled to DPC-6400-22-44 array. Also for that detector the FWHM obtained in the center region of the crystal was a little smaller than 1 mm FWHM, while the FWTM was ∼ 2 mm. Averaged over the entire 24 mm × 24 mm × 10 mm crystal, a FWHM of ∼ 1 mm and a FWTM of ∼ 2.3 mm were achieved. The slightly higher average values obtained in the present work can be attributed to the increased influence of the intermediate and edge regions in a detector with a smaller surface area. Cabello et al. [12] reported a spatial resolution of ∼ 0.7 mm FWHM and ∼ 2.0 mm FWTM for a detector based on a 12 mm × 12 mm × 10 mm LYSO crystal and a 8 × 8 pixels analog SiPM array. These excellent results may have been due to the small photosensor pixel size of 1.5 mm × 1.4 mm, which enables a very fine sampling of the light distribution. Ling et al. [17] achieved a spatial resolution of ∼ 1.1 mm FWHM in the central part of the crystal and ∼ 1.3 mm FWHM in the corners of the detector for a detector based on a 50 mm × 50 mm × 8 mm LYSO crystal and a 64-channel flat-panel PMT.

The results obtained with the 16 mm × 16 mm × 20 mm crystal are considered highly promising since, to our knowledge, this is the first time a FWHM better than 2 mm is achieved with a ≥ 20 mm thick monolithic crystal with back-side readout (BSR). So far, this had only been demonstrated with monolithic scintillator detectors employing double-side readout (DSR) [24]. Previously, the thickest detector having single-side readout which demonstrated a FWHM resolution < 2 mm was the one described by Li et al., in [10], which was based on a 50 mm × 50 mm × 15 mm LYSO crystal and a 64-channel flat-panel PMT and had a spatial resolution of ∼ 1.5 mm FWHM.

Still, the PSFs obtained for the 20 mm thick detector presented in this paper show long tails, which determine the value of ∼ 6 mm for the FWTMs. The tails probably have two causes. The first refers to events for which the gamma-ray undergoes a Compton interaction and is subsequently absorbed in a position distant from the original line of irradiation. Due to the crystal thickness, this distance can be significant in the x- and y- directions even for relatively small scattering angles. The second reason refers to the aspect-ratio of the crystal, which is rather high compared to its width. This crystal shape determines that the cone of direct light (i.e. the photons having an angle of incidence with the photosensors surface smaller than the critical

TABLE III
FWHM AND FWTH VALUES OF REGIONAL PSFS IN THE REGIONS INDICATED IN FIG. 4 FOR THE 16 mm × 16 mm × 10 mm CRYSTAL. THE SMOOTHED 1D AND SMOOTHED 2D k-NN POSITION ESTIMATION ALGORITHMS WERE USED

REGION	X DIRECTION				Y DIRECTION			
	FWHM (mm)		FWTM (mm)		FWHM (mm)		FWTM (mm)	
	1D	2D	1D	2D	1D	2D	1D	2D
Left edge	1.61	1.62	4.10	4.02	1.02	1.03	2.61	2.60
Right edge	1.56	1.39	3.80	3.69	1.00	1.00	2.59	2.53
Upper edge	1.07	1.02	2.57	2.46	1.74	1.38	4.07	3.88
Lower edge	1.01	1.05	2.43	2.44	1.65	1.58	4.08	4.26
Center	0.98	0.97	2.01	1.99	0.99	0.96	2.06	2.02
Intermediate	1.11	1.08	2.55	2.53	1.11	1.13	2.71	2.66
Total	1.08	1.07	2.70	2.63	1.10	1.07	2.75	2.75

TABLE IV
FWHM AND FWTH VALUES OF REGIONAL PSFS IN THE REGIONS INDICATED IN FIG. 4 FOR THE 16 mm × 16 mm × 20 mm CRYSTAL. THE SMOOTHED 1D AND SMOOTHED 2D k-NN POSITION ESTIMATION ALGORITHMS WERE USED

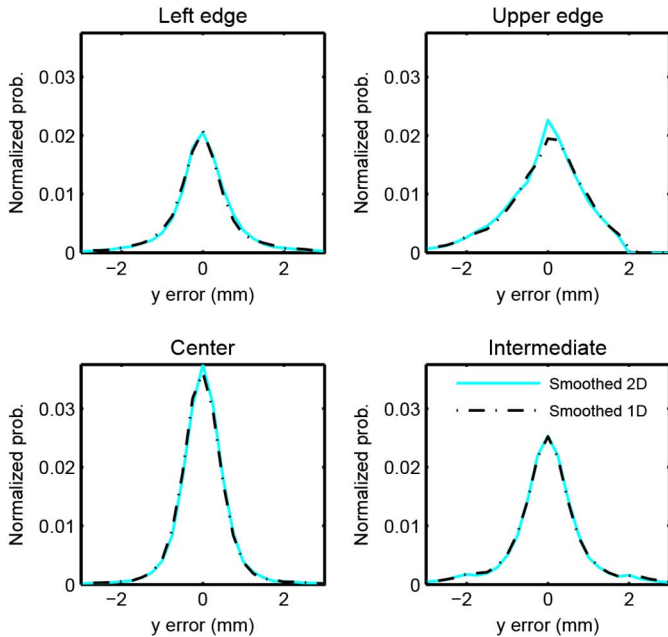| REGION	X DIRECTION				Y DIRECTION			
	FWHM (mm)		FWTM (mm)		FWHM (mm)		FWTM (mm)	
	1D	2D	1D	2D	1D	2D	1D	2D
Left edge	2.13	2.04	6.41	6.21	1.51	1.61	6.02	6.66
Right edge	1.96	1.84	6.26	5.67	1.67	1.54	6.27	6.39
Upper edge	1.59	1.59	6.27	6.25	2.12	1.89	6.92	6.33
Lower edge	1.54	1.42	6.21	5.81	2.21	1.86	7.28	6.63
Center	1.22	1.31	6.24	4.91	1.22	1.29	8.31	5.27
Intermediate	1.54	1.51	6.40	6.48	1.58	1.56	6.73	7.33
Total	1.51	1.49	5.94	5.85	1.57	1.50	6.38	6.22

Fig. 5. Cross-sections in the y-direction through the maximum of the regional PSFs obtained with the 1D (black) and 2D (cyan) Smoothed k-NN methods for the 10 mm thick crystal. From left to right, top to bottom, they correspond to the left-edge region, top-edge region, central region, and intermediate region.
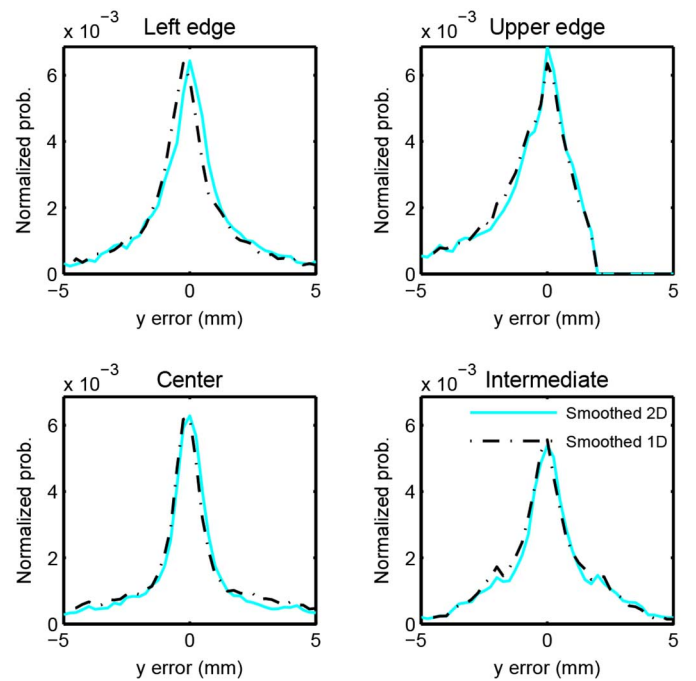

Fig. 6. Cross-sections in the y-direction through the maximum of the regional PSFs obtained with the 1D (black) and 2D (cyan) Smoothed k-NN methods for the 20 mm thick crystal. From left to right, top to bottom, they correspond to the left-edge region, top-edge region, central region, and intermediate region.

angle) created by events taking place in the top part of the crystal is distorted and truncated by reflections on the side surfaces of the crystal. Therefore, the change of the light distribution with position, which determines the lower bound on the variance on

the estimated interaction coordinates [29], [30], becomes worse compared to the situation in a crystal with lower aspect ratio,

where at least one side of the direct light distribution is never truncated. The FWTM values could therefore improve significantly in lower-aspect-ratio crystals.

Looking at the regional PSF of both detectors, it is possible to notice a worsening in the spatial resolution in the edge regions of the crystal compared to the resolution observed in the central region. This deterioration, which happens for both reconstruction methods, is limited to the coordinate perpendicular to the considered edge and is consistent with previous results [10], [11], [14], [25]. A detailed discussion about the causes underlying this phenomenon can be found in [14].

C. Bias

The plots of the bias vectors $\boldsymbol{b}(\boldsymbol{v}_{ij})$, calculated as described in Section II-C) for the Smoothed 1D and the Smoothed 2D methods applied to the 10 mm thick crystal, are shown in Fig. 7. No considerable differences are observed. Only the regions near the corners show a slightly (< 0.3 mm) higher bias towards the center for the Smoothed 1D method. Both of the position estimation methods reach remarkable results; except for the border regions (distance ≤ 1 mm from the edges) the bias is always smaller than 0.5 mm.

For the 20 mm thick crystal (Fig. 8) the bias is ≤ 1.1 mm in the center and intermediate regions for both position estimation methods. The bias becomes more pronounced in the edge regions, where it is between 1 mm and 2 mm, and in the corners, where it can reach almost 4 mm. Also for this detector the Smoothed 1D method shows a slightly higher bias in the corners. The difference with the Smoothed 2D method is ≤ 0.5 mm and occurs at distances of less than 2 mm from the corners only. For this detector, a small difference between the position estimation methods can be noticed in the central region as well; in this area the 1D positioning method seems to perform slightly better.

The hypothesis that the increased bias found with the Smoothed 1D method in the corner regions is due to the non-uniform distribution of the reference events along the lines irradiated with the fan beam has been considered and tested. This non-uniformity is due to the higher escape probability of the scattered photon following a Compton interaction near the edges (see also Section II-C). In principle this could result in a higher possibility to select events from the central region during position estimation, especially in the corner regions. To test this hypothesis, the bias plot was calculated also for the Smoothed 1D$_{\text{ideal}}$ method, which makes use of the reference dataset acquired for the pencil-beam calibration. Since in this calibration procedure the irradiation times are adjusted to acquire the same number of full-energy events in each grid point, the reference dataset used for the Smoothed 1D$_{\text{ideal}}$ method is uniform along each line. However, approximately the same increased bias in the corners was observed also for this dataset and therefore the hypothesis is rejected.

The independent estimation of the x- and the y-coordinates in the Smoothed 1D method therefore seems a more likely cause of the increased bias in the corners. In those regions the variation of light distribution with one of the coordinates probably is no longer independent of the other coordinate and the correlated estimation of the x- and y-coordinates by the Smoothed
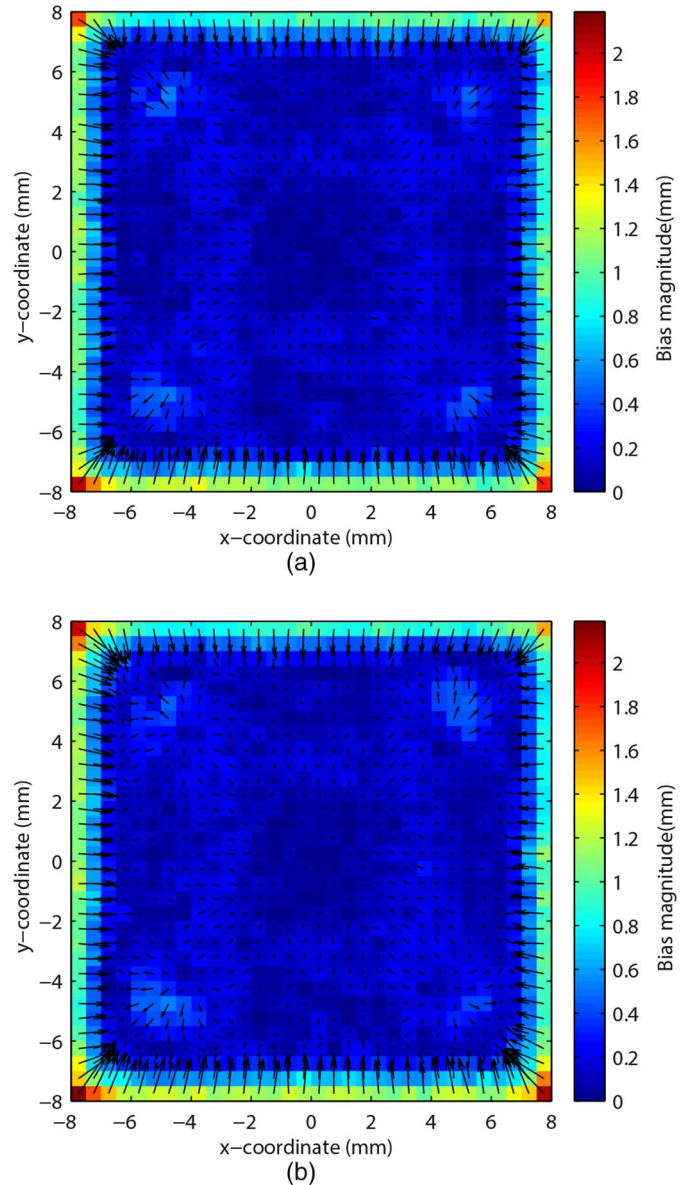

Fig. 7. Direction and magnitude of the bias vectors $\boldsymbol{b}(\boldsymbol{v}_{ij})$ obtained with the Smoothed 1D (a) and the Smoothed 2D (b) position estimation methods for the 10 mm thick crystal. The bias vectors are averaged over an area of 0.5 mm $\times$ 0.5 mm, i.e. over 2×2 irradiation positions. The color scale represents the vector magnitude.

2D method may yield better results. Anyway, the differences in bias between the different calibration methods are small and therefore are not expected to change the detector performance significantly.

IV. CONCLUSIONS

A new method to estimate the position of interaction of 511 keV gamma-photons in monolithic scintillator detectors was tested experimentally for the first time. This method is based on a modified (Smoothed 1D) k-NN algorithm that enables efficient acquisition of reference events by means of a fan beam. The new method was compared to a method based on pencil-beam irradiation (Smoothed 2D) that has previously been shown to give good results in 10 mm thick crystals [11],
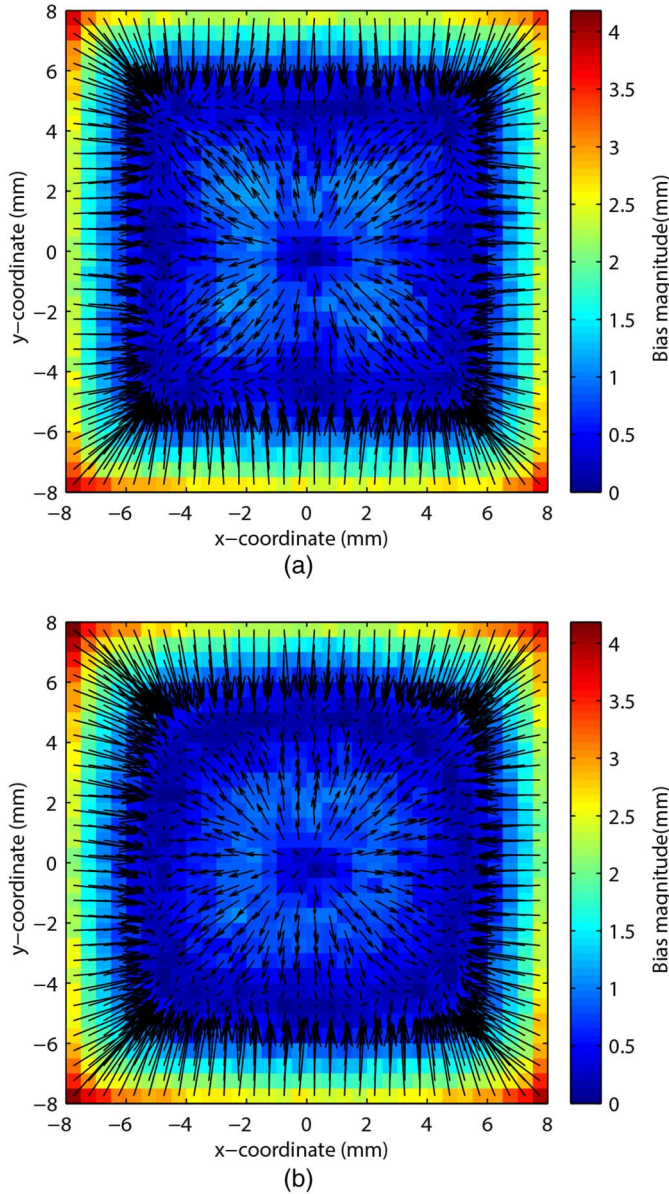
The new calibration method proved to be more than one order of magnitude faster than the previous one using the same point source. Moreover, a fan beam similar to the one used in this experiment could be obtained with a collimated line source. A line source can be produced with a total activity much higher than a point source since the radioactive volume is larger at the same source diameter. Therefore, if necessary, detector calibration could be made even faster if line sources were employed.

The fan-beam method reduces the complexity of the calibration procedure considerably. With a pencil beam the total number of reference positions is $n_{\text{pos}} \times n_{\text{pos}}$, whereas with a fan beam it equals $n_{\text{pos}} + n_{\text{pos}}$ only, where n_{pos} is the number of reference positions along one crystal axis. This is particularly important when implementing a procedure for acquiring the reference events in an assembled PET scanner. Using multiple line-sources in combination with mechanical and/or electronic collimation, irradiation condition similar to those used in this work could be obtained in a PET ring in order to simultaneously calibrate all the detectors. Calibration of a full scanner with pencil beams, instead, would be a much more complex and time consuming task.

In conclusion, the new calibration method may enable the acquisition of reference datasets in a reasonable time period also in a clinical environment. Thus, fan-beam calibration could eliminate the calibration problems that have so far hampered the application of monolithic detectors in clinical PET systems. The actual implementation of such a procedure will require further investigations, e.g. to determine the optimum number of sources and the geometry needed to simultaneously calibrate all the detectors.

APPENDIX
APPENDIX A: MISALIGNMENT CORRECTION

In this experiment, the coordinate systems defined during the pencil-beam irradiation and the fan-beam irradiation could be slightly misaligned. Therefore, to correctly determine the error in the interaction positions estimated with the Max 1D and Smoothed 1D methods,. the irradiation positions of the reference events, i.e. the possible estimated positions, have to be determined in the coordinate system of the test events.

Let us define the coordinate system used during the fan-beam irradiation as $X''Y''$ and the coordinate system used during the pencil-beam irradiation as XY (see Fig. 9). Both of them are centered approximately in the center of the crystal. The misalignment between them can be described as a linear coordinate transformation. The corresponding translation vector $\boldsymbol{t} = (t_x, t_y)$ and the rotation angle α can be determined using the following assumption. If the calibration and test coordinates are aligned perfectly, then the x-error distributions for two positions that are located symmetrically with respect to the crystal y-axis should be symmetric with respect to the zero error axis. The mean value of their summed error distributions should therefore be 0. Similar arguments apply in the orthogonal direction. Therefore, if the crystal is irradiated at a rectangular grid of positions uniformly distributed over a rectangular region centered on the crystal center, the mean x-error on each grid row, the mean y-error on each grid column, and, therefore, the total

Fig. 8. Direction and magnitude of the bias vectors $\boldsymbol{b}(\boldsymbol{v_{ij}})$ obtained with the Smoothed 1D (a) and the Smoothed 2D (b) position estimation methods for the 20 mm thick crystal. The bias vectors are averaged over an area of 0.5 mm × 0.5 mm, i.e. over 2 × 2 irradiation positions. The color scale represents the vector magnitude.

[14], [23]. The new method was tested using two detectors based on DPC arrays and LSO:Ce (0.2%Ca) monolithic crystals having dimensions of 16 mm × 16 mm × 10 mm and 16 mm × 16 mm × 20 mm.

With both crystals, the Smoothed 1D method essentially achieved the same performance as the Smoothed 2D method with respect to the overall spatial resolution, the spatial resolution of selected detector regions, and the positioning bias. With the 10 mm thick crystal, an overall spatial resolution of ∼ 1.1 mm FWHM and ∼ 2.7 mm FWTM was achieved, whereas a FWHM of ∼ 1.5 mm and a FWTM of ∼ 6 mm were obtained with the 20 mm thick crystal.
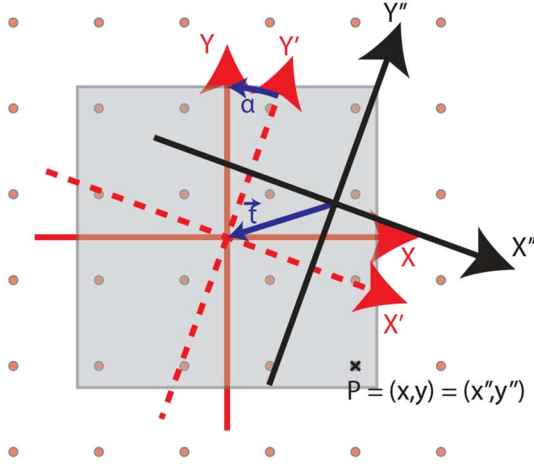
Fig. 9. Sketch of the transformation of the coordinate system applied to the estimated positions of the test events obtained with the fan-beam methods, to make them consistent with the positions of the pencil-beam irradiation; $X''Y''$ is the coordinate system used during the fan-beam irradiation and XY is the coordinate system used during the pencil-beam irradiation. The red dots represents the grid positions of the pencil-beam irradiation and the grey square contains the grid positions selected for the correction.

mean error, should be zero. Even if the reference and test grids are slightly rotated and/or translated with respect to the crystal edges, this assumption still holds within good approximation in the crystal region that is not affected by significant bias (see Section II-C) for a definition of bias). Therefore, a potential translation between the reference and test coordinate systems can be corrected by imposing:

$$
e = \begin{bmatrix} \frac{\sum_{i,j,m}\left(\left(\hat{x}''_m(\boldsymbol{v}_{i,j})-t_x\right)-x_{i,j}\right)}{I \times J \times M} \\ \frac{\sum_{i,j,m}\left(\left(\hat{y}''_m(\boldsymbol{v}_{i,j})-t_y\right)-y_{i,j}\right)}{I \times J \times M} \end{bmatrix} = 0, \qquad (2)
$$

where m is the mth test event at position $\boldsymbol{v}_{i,j} = (x_{i,j}, y_{i,j})$ (i and j being the row and column indexes of the grid), $\hat{\boldsymbol{v}}''_m = (\hat{x}''_m, \hat{y}''_m)$ is its estimated position, M is the number of events per positions, and I and J are the number of grid positions in the x- and y-direction, respectively.

Subsequently, a potential rotation R_α can be estimated from the sum of the x-errors on each grid row and of the y-errors on each grid column. The angle α can be determined as:

$$
\alpha = \arg\min_\alpha \left\{ \sum_i \left| \frac{\sum_{j,m} R_\alpha\left(\hat{x}'_m(\boldsymbol{v}_{i,j})\right)-x_{i,j}}{I \times J \times M} \right| \right.
$$
$$
\left. + \sum_j \left| \frac{\sum_{i,m} R_\alpha\left(\hat{y}'_m(\boldsymbol{v}_{i,j})\right)-y_{i,j}}{I \times J \times M} \right| \right\}. \qquad (3)
$$

Previous studies [11], [14] showed that the central region of monolithic detectors is usually not affected significantly by bias. Therefore, the events acquired during the pencil-beam irradiation having coordinates x and y between -4 mm and 4 mm from the crystal center (in the system of coordinate XY of the pencil-beam irradiation) were selected to calculate the corrections for the Max 1D and the Smoothed 1D k-NN methods in both the crystals.

TABLE V
COMPONENTS OF THE TRANSLATION VECTOR $\boldsymbol{t} = (\boldsymbol{t_x}, \boldsymbol{t_y})$ AND ROTATION ANGLE α NECESSARY TO ALIGN THE COORDINATE SYSTEMS USED DURING THE PENCIL-BEAM SAN AND THE FAN-BEAM SCAN

CRYSTAL	METHOD	t_x (mm)	t_y (mm)	$\alpha°$
16 mm × 16 mm × 10 mm	Max 1D	-0.04	-0.11	0.96
	Smoothed 1D	-0.04	-0.11	0.93
16 mm × 16 mm × 20 mm	Max 1D	0.00	-0.05	0.00
	Smoothed 1D	-0.01	-0.04	0.00

The components of the translation vector $\boldsymbol{t} = (t_x, t_y)$ and the rotation angle α necessary to align the coordinate systems of the fan-beam scans to the coordinate systems of the pencil-beam scans are given in Table V for both of the 1D methods. For both crystals the values obtained with the two different algorithms are consistent.

REFERENCES

[1] P. Bruyndonckx, C. Lemaitre, S. Leonard, D. R. Schaart, D. J. van der Laan, M. C. Maas, O. Devroede, W. Yibao, M. Krieguer, and S. Tavernier, "Initial haracterization of a nonpixelated scintillator detector in a PET prototype demonstrator," *IEEE Trans. Nucl. Sci.*, vol. 53, no. 5, pp. 2543–2548, Oct. 2006.
[2] M. C. Maas, D. Van der Laan, D. R. Schaart, J. Huizenga, J. C. Brouwer, P. Bruyndonckx, S. Leonard, C. Lemaitre, and C. W. E. van Eijk, "Experimental characterization of monolithic-crystal small animal PET detectors read out by APD arrays," *IEEE Trans. Nucl. Sci.*, vol. 53, no. 3, pp. 1071–1077, Jun. 2006.
[3] R. S. Miyaoka, L. Xiaoli, W. Hunter, L. A. Pierce, W. McDougald, P. E. Kinahan, and T. K. Lewellen, "Resolution properties of a prototype continuous miniature crystal element (cMiCE) scanner," *IEEE Trans. Nucl. Sci.*, vol. 58, no. 5, pp. 2244–2249, Oct. 2011.
[4] M. Carles, C. W. Lerche, F. Sánchez, A. Orero, L. Moliner, A. Soriano, and J. M. Benlloch, "Performance of a DOI-encoding small animal PET system with monolithic scintillators," *Nucl. Instrum. Methods Phys. Res. A*, vol. 695, pp. 317–321, 2012.
[5] G. Llosá, P. Barrillon, J. Barrio, M. G. Bisogni, J. Cabello, A. Del Guerra, A. Etxebeste, J. E. Gillam, C. Lacasta, J. F. Oliver, M. Rafecas, C. Solaz, V. Stankova, and C. de La Taille, "High performance detector head for PET and PET/MR with continuous crystals and SiPMs," *Nucl. Instrum. Methods Phys. Res. A*, vol. 702, pp. 3–5, 2013.
[6] I. Sarasola, P. R. Mendes, P. Garcia de Acilu, M. Canadas, O. Vela, J. M. Cela, J. C. Oller, L. Nunez, C. Willmott, and J. M. Perez, "PET Demonstrator for a human brain scanner based on monolithic detector blocks," *IEEE Trans. Nucl. Sci.*, vol. 58, no. 5, pp. 2190–2197, Oct. 2011.
[7] M. Kaul, S. Surti, and J. S. Karp, "Combining surface treatments with shallow slots to improve the spatial resolution performance of continuous, Thick LYSO detectors for PET," *IEEE Trans. Nucl. Sci.*, vol. 60, no. 1, pp. 44–52, Feb. 2013.
[8] G. Llosá, J. Cabello, S. Callier, J. E. Gillam, C. Lacasta, M. Rafecas, L. Raux, C. Solaz, V. Stankova, C. de La Taille, M. Trovato, and J. Barrio, "First Compton telescope prototype based on continuous LaBr3-SiPM detectors," *Nucl. Instrum. Methods Phys. Res. A*, vol. 718, pp. 130–133, 2013.
[9] S. España, K. Deprez, R. V. Holen, and S. Vandenberghe, "Fast calibration of SPECT monolithic scintillation detectors using un-collimated sources," *Phys. Med. Biol.*, vol. 58, pp. 4807–4825, 2013.
[10] L. Xiaoli, W. C. J. Hunter, T. K. Lewellen, and R. S. Miyaoka, "Use of Cramer-Rao Lower bound for performance evaluation of different monolithic crystal PET detector designs," *IEEE Trans. Nucl. Sci.*, vol. 59, no. 1, pp. 3–12, Feb. 2012.
[11] S. Seifert, G. v. d. Lei, H. T. v. Dam, and D. R. Schaart, "First characterization of a digital SiPM based time-of-flight PET detector with 1 mm spatial resolution," *Phys. Med. Biol.*, vol. 58, pp. 3061–3074, 2013.
[12] J. Cabello, P. Barrillon, J. Barrio, M. G. Bisogni, A. Del Guerra, C. Lacasta, M. Rafecas, H. Saikouk, C. Solaz, P. Solevi, C. de La Taille, and G. Llosá, "High resolution detectors based on continuous crystals and SiPMs for small animal PET," *Nucl. Instrum. Methods Phys. Res. A*, vol. 718, pp. 148–150, 2013.

[13] H. T. van Dam, G. Borghi, S. Seifert, and D. R. Schaart, "Sub-200 ps CRT in monolithic scintillator PET detectors using digital SiPM arrays and maximum likelihood interaction time estimation," *Phys. Med. Biol.*, vol. 58, pp. 3243–3257, 2013.

[14] S. Seifert, H. T. v. Dam, J. Huizenga, R. Vinke, P. Dendooven, H. Löhner, and D. R. Schaart, "Monolithic LaBr3:Ce crystals on silicon photomultiplier arrays for time-of-flight positron emission tomography," *Phys. Med. Biol.*, vol. 57, pp. 2219–2233, 2012.

[15] C. W. Lerche, J. M. Benlloch, F. Sanchez, N. Pavon, B. Escat, E. N. Gimenez, M. Fernandez, I. Torres, M. Gimenez, A. Sebastia, and J. Martinez, "Depth of gamma-ray interaction within continuous crystals from the width of its scintillation light-distribution," *IEEE Trans. Nucl. Sci.*, vol. 52, no. 3, pp. 560–572, Jun. 2005.

[16] T. Ling, T. K. Lewellen, and R. S. Miyaoka, "Depth of interaction decoding of a continuous crystal detector module," *Phys. Med. Biol.*, vol. 52, pp. 2213–2228, 2007.

[17] T. Ling, T. H. Burnett, T. K. Lewellen, and R. S. Miyaoka, "Parametric positioning of a continuous crystal PET detector with depth of interaction decoding," *Phys. Med. Biol.*, vol. 53, pp. 1843–1863, 2008.

[18] W. C. J. Hunter, H. H. Barrett, and L. R. Furenlid, "Calibration method for ML estimation of 3D interaction position in a thick gamma-ray detector," *IEEE Trans. Nucl. Sci.*, vol. 56, no. 1, pp. 189–196, Feb. 2009.

[19] Z. Li, M. Wedrowski, P. Bruyndonckx, and G. Vandersteen, "Nonlinear least-squares modeling of 3D interaction position in a monolithic scintillator block," *Phys. Med. Biol.*, vol. 55, pp. 6515–6532, 2010.

[20] H. T. van Dam, S. Seifert, R. Vinke, P. Dendooven, H. Löhner, F. J. Beekman, and D. R. Schaart, "A practical method for depth of interaction determination in monolithic scintillator PET detectors," *Phys. Med. Biol.*, vol. 56, pp. 4135–4145, 2011.

[21] P. Bruyndonckx, S. Leonard, S. Tavernier, C. Lemaitre, O. Devroede, Y. Wu, and M. Krieguer, "Neural network-based position estimators for PET detectors using monolithic LSO blocks," *IEEE Trans. Nucl. Sci.*, vol. 51, no. 5, pp. 2520–2525, Oct. 2004.

[22] P. Bruyndonckx, C. Lemaitre, D. J. van der Laan, M. Maas, D. Schaart, W. Yonggang, L. Zhi, M. Krieguer, and S. Tavernier, "Evaluation of machine learning algorithms for localization of photons in undivided scintillator blocks for PET detectors," *IEEE Trans. Nucl. Sci.*, vol. 55, no. 3, pp. 918–924, Jun. 2008.

[23] H. T. van Dam, S. Seifert, R. Vinke, P. Dendooven, H. Löhner, F. J. Beekman, and D. R. Schaart, "Improved nearest neighbor methods for gamma photon interaction position determination in monolithic scintillator PET detectors," *IEEE Trans. Nucl. Sci.*, vol. 58, no. 5, pp. 2139–2147, Oct. 2011.

[24] M. C. Maas, D. R. Schaart, D. J. v. d. Laan, P. Bruyndonckx, C. Lemaître, F. J. Beekman, and C. W. E. van Eijk, "Monolithic scintillator PET detectors with intrinsic depth-of-interaction correction," *Phys. Med. Biol.*, vol. 54, pp. 1893–1908, 2009.

[25] D. R. Schaart, H. T. v. Dam, S. Seifert, R. Vinke, P. Dendooven, H. Löhner, and F. J. Beekman, "A novel, SiPM-array-based, monolithic scintillator detector for PET," *Phys. Med. Biol.*, vol. 54, pp. 3501–3512, 2009.

[26] T. Frach, G. Prescher, C. Degenhardt, R. de Gruyter, A. Schmitz, and R. Ballizany, "The digital silicon photomultiplier - Principle of operation and intrinsic detector performance," in *Proc. IEEE Nuclear Science Symp. Conf. Rec.*, Orlando, FL, USA, 2009, pp. 1959–1965.

[27] T. Frach, G. Prescher, C. Degenhardt, and B. Zwaans, "The digital silicon photomultiplier - System architecture and performance evaluation," in *Proc. IEEE Nuclear Science Symp. Conf. Rec.*, Knoxville, TN, USA, 2010, pp. 1722–1727.

[28] M. A. Spurrier, P. Szupryczynski, Y. Kan, A. A. Carey, and C. L. Melcher, "Effects of Ca2+ Co-doping on the scintillation properties of LSO:Ce," *IEEE Trans. Nucl. Sci.*, vol. 55, no. 3, pp. 1178–1182, Jun. 2008.

[29] D. Van der Laan, M. C. Maas, D. R. Schaart, P. Bruyndonckx, S. Leonard, and C. W. E. Van Eijk, "Using Cramer-Rao theory combined with Monte Carlo simulations for the optimization of monolithic scintillator PET detectors," *IEEE Trans. Nucl. Sci.*, vol. 53, no. 3, pp. 1063–1070, Jun. 2006.

[30] D. J. v. d. Laan, M. C. Maas, P. Bruyndonckx, and D. R. Schaart, "Limits on the spatial resolution of monolithic scintillators read out by APD arrays," *Phys. Med. Biol.*, vol. 57, pp. 6479–6496, 2012.